NeuroImage 264 (2022) 119680

Contents lists available at ScienceDirect

NeuroImage

journal homepage: www.elsevier.com/locate/neuroimage

A unified model for reconstruction and R_2^* mapping of accelerated 7T data using the quantitative recurrent inference machine

Chaoping Zhang [a,b,c], Dimitrios Karkalousos [a,b], Pierre-Louis Bazin [d,e], Bram F. Coolen [a], Hugo Vrenken [b,f], Jan-Jakob Sonke [c], Birte U. Forstmann [d], Dirk H.J. Poot [g], Matthan W.A. Caan [a,b,h,*]

[a] Amsterdam UMC location University of Amsterdam, Biomedical Engineering and Physics, Meibergdreef 9, Amsterdam, the Netherlands
[b] Amsterdam Neuroscience, Brain Imaging, Amsterdam, the Netherlands
[c] Netherlands Cancer Institute, Amsterdam, the Netherlands
[d] Integrative Model-based Cognitive Neuroscience Research unit, University of Amsterdam, Amsterdam, the Netherlands
[e] Max Planck Institute for Human Cognitive and Brain Sciences, Leipzig, Germany
[f] Amsterdam UMC location Vrije Universiteit Amsterdam, Department of Radiology, De Boelelaan 1117, Amsterdam, the Netherlands
[g] Biomedical Imaging Group Rotterdam, Department of Radiology & Nuclear Medicine, Erasmus MC, Rotterdam, the Netherlands
[h] Computational Radiology and Artificial Intelligence, Division of Radiology and Nuclear Medicine, Oslo University Hospital, Oslo, Norway

ARTICLE INFO

Keywords:
Magnetic resonance imaging
Quantitative MRI
Image reconstruction
R_2^* mapping
Deep learning
Subcortex

ABSTRACT

Quantitative MRI (qMRI) acquired at the ultra-high field of 7 Tesla has been used in visualizing and analyzing subcortical structures. qMRI relies on the acquisition of multiple images with different scan settings, leading to extended scanning times. Data redundancy and prior information from the relaxometry model can be exploited by deep learning to accelerate the imaging process. We propose the quantitative Recurrent Inference Machine (qRIM), with a unified forward model for joint reconstruction and R_2^*-mapping from sparse data, embedded in a Recurrent Inference Machine (RIM), an iterative inverse problem-solving network. To study the dependency of the proposed extension of the unified forward model to network architecture, we implemented and compared a quantitative End-to-End Variational Network (qE2EVN). Experiments were performed with high-resolution multi-echo gradient echo data of the brain at 7T of a cohort study covering the entire adult life span. The error in reconstructed R_2^* from undersampled data relative to reference data significantly decreased for the unified model compared to sequential image reconstruction and parameter fitting using the RIM. With increasing acceleration factor, an increasing reduction in the reconstruction error was observed, pointing to a larger benefit for sparser data. Qualitatively, this was following an observed reduction of image blurriness in R_2^*-maps. In contrast, when using the U-Net as network architecture, a negative bias in R_2^* in selected regions of interest was observed. Compressed Sensing rendered accurate, but less precise estimates of R_2^*. The qE2EVN showed slightly inferior reconstruction quality compared to the qRIM but better quality than the U-Net and Compressed Sensing. Subcortical maturation over age measured by a linearly increasing interquartile range of R_2^* in the striatum was preserved up to an acceleration factor of 9. With the integrated prior of the unified forward model, the proposed qRIM can exploit the redundancy among repeated measurements and shared information between tasks, facilitating relaxometry in accelerated MRI.

1. Introduction

The human subcortex is involved in complex activities of normal behavior and physiology, e.g., in decision-making (Ding and Gold, 2013), reward processing (O'Doherty et al., 2004; Schultz et al., 1997), and motor behavior (Mink, 1996). Magnetic resonance imaging (MRI) has been an important tool in researching subcortical structures. At lower field-strength, this has however been challenging due to the large number, small size and close spatial proximity of the structures (Keuken et al., 2018).

* Corresponding author at: Amsterdam UMC, University of Amsterdam, Biomedical Engineering and Physics, Meibergdreef 9, 1105 AZ, Amsterdam, the Netherlands.
E-mail addresses: c.zhang@nki.nl (C. Zhang), d.karkalousos@amsterdamumc.nl (D. Karkalousos), pilou.bazin@uva.nl (P.-L. Bazin), b.f.coolen@amsterdamumc.nl (B.F. Coolen), h.vrenken@amsterdamumc.nl (H. Vrenken), j.sonke@nki.nl (J.-J. Sonke), B.U.Forstmann@uva.nl (B.U. Forstmann), d.poot@erasmusmc.nl (D.H.J. Poot), m.w.a.caan@amsterdamumc.nl (M.W.A. Caan).

https://doi.org/10.1016/j.neuroimage.2022.119680.
Received 30 March 2022; Received in revised form 16 September 2022; Accepted 10 October 2022
Available online 12 October 2022.
1053-8119/© 2022 The Authors. Published by Elsevier Inc. This is an open access article under the CC BY-NC-ND license (http://creativecommons.org/licenses/by-nc-nd/4.0/)

The advent of ultra-high field 7 Tesla MRI has fundamentally changed the opportunities for subcortical imaging. First, by increased Signal-to-Noise Ratio (SNR), image acquisition at an unprecedented level of detail has become possible. Second, the field strength dependence of relaxometry parameters such as R_2^* has enabled identification and parcellation of subcortical structures (Bazin et al., 2020a; Keuken et al., 2018). By performing quantitative magnetic resonance imaging (qMRI), intrinsic tissue properties are measured, in which the resulting values are independent of the specific MRI sequence parameters (Tofts, 2005). The quantitative metrics allow for cross-sectionally monitoring of subtle changes over the life span and longitudinally in disease progression. Quantitative 7T MRI has thus set a new standard in visualizing subcortical structures (Alkemade et al., 2020).

The relaxation parameter R_2^* measures the effective spin-spin relaxation rate of tissues and finds its application in image-guided Deep Brain Stimulation for Parkinson's disease (Isaacs et al., 2020), and detection of hemorrhage, micro-calcifications, and iron deposits (Stüber et al., 2014). These iron deposits are a marker of maturation, as they are known to accumulate with increasing age, leading to an increasing inhomogeneous appearance of R_2^* in deep nuclei. The interquartile range of R_2^* in e.g. the striatum shows a strong linear correlation with age (Miletić et al., 2022). This demonstrates the joint added benefit of increased R_2^*-contrast and ultra high-resolution imaging at 7T.

Quantitative maps of tissue properties typically need the acquisition of multiple images with different specifications (Tofts, 2005). Conventionally, R_2^* is fitted from reconstructed images of multiple echo times acquired with a multi-echo gradient echo (ME-GRE) sequence. While conventional ultra-high resolution MRI acquisitions are already time-consuming, scanning the multiple images under varying relaxometry conditions necessary for qMRI may take even longer. This often exceeds the acceptable time in the clinic and can make imaging vulnerable to involuntary subject motion (Andre et al., 2015).

Imaging may be accelerated by acquiring fewer samples in k-space, resulting in sparse data, for which multiple reconstruction methods have been proposed. Parallel imaging (Griswold et al., 2002; Pruessmann et al., 1999) is well established, which with its more recent variants such as SPIRiT (Lustig and Pauly, 2010), ESPIRiT (Uecker et al., 2014), LORAKS (Haldar, 2013), and joint virtual coil reconstructions (Bilgic et al., 2018; Zhang et al., 2021; 2020) makes use of the extra spatial encoding from multi-channel receive coils. Compressed sensing (Bilgic et al., 2011; Chatnuntawech et al., 2016; Ehrhardt and Betcke, 2016; Haldar et al., 2011; Kopanoglu et al., 2020; Küstner et al., 2016; Lustig et al., 2008; Maier et al., 2019) and dictionary learning based methods (Caballero et al., 2014; Huang et al., 2014; Ravishankar and Bresler, 2010; Rueda et al., 2013; Wang and Ying, 2014; Zhan et al., 2015) further exploit the image prior of sparsity in a sparsifying domain, e.g., by the wavelet transform, total variation, or adaptively learned dictionary transform of the image.

Following up, deep learning-based methods have been proposed, aiming to further accelerate imaging. Deep neural networks can approximate a prior customized to the task of MRI reconstruction by learning from training data. Deep learning has set the state-of-the-art performance in multiple reconstruction tasks recently (Knoll et al., 2020; Liang et al., 2020; Muckley et al., 2021). Defining an optimization problem for reconstruction, the iterative optimization process can be unrolled into deep networks (Gregor and LeCun, 2010), or approached with the recurrent neural networks (Putzky and Welling, 2017). Following up, it was understood that deep learning-based reconstruction may benefit from the physics-based known forward model for image reconstruction. Typically, this model is formulated in the optimization problem and embedded in the learning and inference processes, e.g., in the variational networks (Hammernik et al., 2018) and the Recurrent Inference Machine (RIM) (Lønning et al., 2019), among others (Schlemper et al., 2017; Aggarwal et al., 2018; Tezcan et al., 2019; Wang et al., 2020).

While the acceleration techniques in weighted imaging treat acquisitions independently, qMRI gives the unique opportunity to further accelerate imaging thanks to the shared information implicitly embedded in repeated acquisitions. In qMRI applications, the domain prior knowledge provided by a compact forward model that maps the parameters directly into the k-space can be exploited. This has been done in pioneering works such as in compressed sensing (Doneva et al., 2010), low-rank reconstruction (Lee et al., 2016), and through an end-to-end convolutional neural network (Liu et al., 2019). Recent work showed the feasibility in the context of T_1-mapping using an unfolded network (Jun et al., 2021).

In this paper, we present the quantitative Recurrent Inference Machine (qRIM) for reconstructing accurate and precise R_2^* maps from highly accelerated high-resolution 7T data. To this end, we adopt a physical model jointly describing the parametric model and image reconstruction. This model describes the expected signal in k-space given R_2^* while accommodating field inhomogeneities. We embed this model in a RIM network towards better exploitation of the implicit correlation over the multiple images in the acquisition. Specifically, with the unified forward physical model, we adopt the convolutional RIM network (Lønning et al., 2019) to directly reconstruct the parameter map from the subsampled k-space. We also implicitly exploit the signal correlation within a vicinity of the voxel through the receptive field of the network. We thereby aim to avoid large errors due to amplified noise at the voxel level in sparsely sampled data at ultrahigh resolution. An overview of the proposed framework for accelerated R_2^*-mapping is given in Fig. 1.

The qRIM network is trained on motion-corrected raw data of the Amsterdam Ultra-high field adult lifespan database (AHEAD) (Alkemade et al., 2020). Experiments are performed to assess accuracy and precision in R_2^* for increasing acceleration factors. Furthermore, we perform a validation experiment into subcortical maturation, taking the increasingly inhomogeneous appearance of R_2^* with age in the striatum as an implicit resolution marker. We expect the qRIM to be better able to maintain tissue structure while reducing imaging noise compared to conventional reconstruction.

Since the extension of the unified forward model is in general applicable to the physics-informed deep networks that wrap an unrolled optimization, we also extended the proposed framework in the state-of-the-art End-to-End Variational Network (Sriram et al., 2020) as comparison.

The remainder of the paper is organized as follows. Section 2 presents the joint optimization problem of a unified model of image reconstruction and relaxation for R_2^* mapping. Section 3 explains the quantitative RIM that is customized to estimate R_2^* with the unified model. Section 4 explains the Quantitative End-to-End Variational Network with the extended unified forward model. Section 5 describes the datasets, the RIM network architecture, and the details of training and evaluation of which the results are presented in Section 6. Following a discussion in Section 7, the conclusions are drawn in Section 8.

2. Theory

2.1. Unified model

In order to define a unified forward model from the quantitative relaxation parameter map R_2^* to k-space coil signals, let us first introduce the R_2^* relaxation model.

In qMRI, multiple images are acquired in the same subject with different acquisition parameters in order to obtain quantitative parameter maps. Specifically, for R_2^* estimation with the ME-GRE sequence, images of multiple echoes are acquired. With noise neglected, the measured complex-valued image $\boldsymbol{x}_t \in \mathbb{C}^P$ of P voxels at echo t with echo time TE_t follows this forward relaxation model:

$$\boldsymbol{x}_t = \boldsymbol{M} \odot \mathrm{e}^{-TE_t(\boldsymbol{R}_2^* - \boldsymbol{B}_0 i)}, \tag{1}$$

where $\boldsymbol{M} \in \mathbb{C}^P$ is the net magnetization, and $\odot$ represents Hadamard product. $\boldsymbol{R}_2^* \in \mathbb{R}^P$ is the parameter map of R_2^* and $\boldsymbol{B}_0 \in \mathbb{R}^P$ is the off-

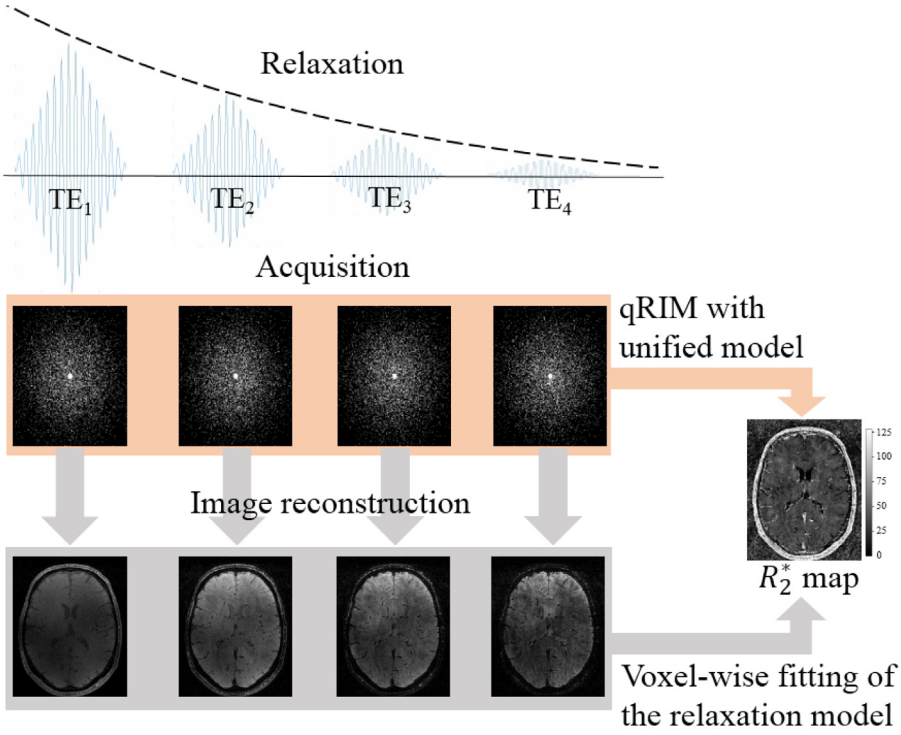

Fig. 1. An overview of the conventional parameter fitting pathway (via gray arrows) and our proposed pathway (via the orange arrow), in application to $\boldsymbol{R}_2^*$-mapping. In qMRI, each echo time in the echo train is filled into its individual k-space. The conventional pathway performs image reconstruction from k-space of every echo time and subsequently voxel-wise fitting of the relaxation model from the reconstructed images, while our proposed method performs simultaneous reconstruction and relaxation model fitting with the unified model and computes the optimized parameter maps from k-space using the quantitative Recurrent Inference Machine (qRIM).

resonance of the static magnetic field, and the exponent is taken element wise.

Providing the known image $\boldsymbol{x}_t$ and following the forward model of image reconstruction for acquisition with a multi-channel receive coil, the corresponding k-space of coil channel c is given by

$$\boldsymbol{y}_{t,c} = G\mathcal{F}\boldsymbol{S}_c\boldsymbol{x}_t + \boldsymbol{n}_{t,c}, \tag{2}$$

where the image $\boldsymbol{x}_t$ is sensed by coil channel c with the sensitivities contained in a diagonal matrix $\boldsymbol{S}_c \in \mathbb{C}^{P\times P}$, and Fourier transformed in k-space signals by $\mathcal{F}$, followed by the subsampling operation $G \in \{0,1\}^{Q\times P}$, $Q \ll P$, with exactly one nonzero in each row and usually not more than one nonzero in each column, which is a common practice for accelerating the imaging. $\boldsymbol{n}_{t,c} \in \mathbb{C}^Q$ is the noise of the sampled positions for echo t in coil channel c.

Substituting Eq. (1) into Eq. (2), we unify the relaxation model and the forward model of image reconstruction as

$$\boldsymbol{y}_{t,c} = G\mathcal{F}\boldsymbol{S}_c(\boldsymbol{M}\odot \mathrm{e}^{-TE_t(\boldsymbol{R}_2^*-\boldsymbol{B}_0 i)}) + \boldsymbol{n}_{t,c}. \tag{3}$$

This unified forward model facilitates mapping from our parameters of interest, i.e., $\boldsymbol{R}_2^*$, $\boldsymbol{M}$, and $\boldsymbol{B}_0$, to k-space signals $\boldsymbol{y}$.

2.2. Problem formulation

With the unified forward model, we aim to estimate the parameters $\boldsymbol{\Phi} = \{\boldsymbol{R}_2^*, \boldsymbol{M}, \boldsymbol{B}_0\}$ from k-space $\boldsymbol{y}$. From the perspective of maximum a posteriori (MAP) estimation, this inverse problem is solved by maximizing the sum of the log-likelihood and log-prior distributions:

$$\hat{\boldsymbol{\Phi}} = \arg\max_{\boldsymbol{\Phi}} \{\log p(\boldsymbol{y}|\boldsymbol{\Phi}) + \log p(\boldsymbol{\Phi})\}. \tag{4}$$

The (negative) log-likelihood $\log p(\boldsymbol{y}|\boldsymbol{\Phi})$ is derived as data consistency between the measured k-space $\boldsymbol{y}$ and the prediction through Eq. (3) with the estimated parameters:

$$\log p(\boldsymbol{y}|\hat{\boldsymbol{\Phi}}) = \frac{1}{\sigma^2}\sum_{t=1}^{T}\sum_{c=1}^{C}\left\| G\mathcal{F}\boldsymbol{S}_c(\hat{\boldsymbol{M}}\odot \mathrm{e}^{-TE_t(\hat{\boldsymbol{R}}_2^*-\hat{\boldsymbol{B}}_0 i)}) - \boldsymbol{y}_{t,c}\right\|_2^2. \tag{5}$$

The log-prior $\log p(\boldsymbol{\Phi})$ can be seen as a regularizer, acting dependent on how the prior knowledge is modeled. For example, in compressed sensing, it is commonly regarded as the $l1$-norm of sparsity of parameters in sparsity domains. In deep learning based methods it can be the network trained from datasets with similar distributions as the target data.

3. Quantitative recurrent inference machine

The Recurrent Inference Machine can be seen as an iterative inverse problem solver (Putzky and Welling, 2017). Here, training the RIM aims to train a network that learns how to estimate $\boldsymbol{R}_2^*$ from k-space data. The RIM is recurrent in nature. While commonly recurrency in neural networks is adopted for modeling time signals, here this architecture is exploited for iterative problem solving. Through a single set of reused network parameters, the network is highly efficient. Still, network complexity is implicitly increased through the iterations. The hidden states, which do vary over iterations, allow the network to pay attention to different regions over the image.

To solve the inverse problem of Eq. (4), with an iterative approach to the MAP inference, $\boldsymbol{\Phi}$ is recursively computed as

$$\boldsymbol{\Phi}_{\tau+1} = \boldsymbol{\Phi}_\tau + \gamma_\tau \nabla(\log p(\boldsymbol{y}|\boldsymbol{\Phi}) + \log p(\boldsymbol{\Phi}))(\boldsymbol{\Phi}_\tau), \tag{6}$$

where γ_τ is the step size at iteration τ. With an explicit forward model, following the framework of the Recurrent Inference Machine this update function can be generalized as Putzky and Welling (2017)

$$\boldsymbol{\Phi}_{\tau+1} = \boldsymbol{\Phi}_\tau + h(\nabla \log p(\boldsymbol{y}|\boldsymbol{\Phi})(\boldsymbol{\Phi}_\tau), \boldsymbol{\Phi}_\tau, \boldsymbol{s}_\tau), \tag{7}$$

where h is a learnable network model that implicitly learns both the scheduling of the step size and the gradient of the prior. The gradient of the log-likelihood encodes the domain knowledge with the included forward model, and is kept as an input. A latent memory variable $\boldsymbol{s}_\tau$ is added to maintain the framework of the recurrent neural network. The update equation of $\boldsymbol{s}_\tau$ given by $\boldsymbol{s}_{\tau+1} = g(\log p(\boldsymbol{y}|\boldsymbol{\Phi})(\boldsymbol{\Phi}_\tau), \boldsymbol{\Phi}_\tau, \boldsymbol{s}_\tau)$ with initialization $\boldsymbol{s}_0 = \boldsymbol{0}$, where g is a learnable update model for $\boldsymbol{s}$.

For computing the gradient of the log-likelihood, we reparameterize the forward model by $\boldsymbol{R} = \boldsymbol{R}_2^* - \boldsymbol{B}_0 i$, and essentially estimate $\boldsymbol{M}, \boldsymbol{R} \in \mathbb{C}^P$ in practice, instead of $\boldsymbol{M} \in \mathbb{C}^P$, and $\boldsymbol{R}_2^*, \boldsymbol{B}_0 \in \mathbb{R}^P$, to facilitate Wirtinger derivatives (Kreutz-Delgado, 2009). The estimates of $\boldsymbol{R}_2^*$ and $\boldsymbol{B}_0$ can

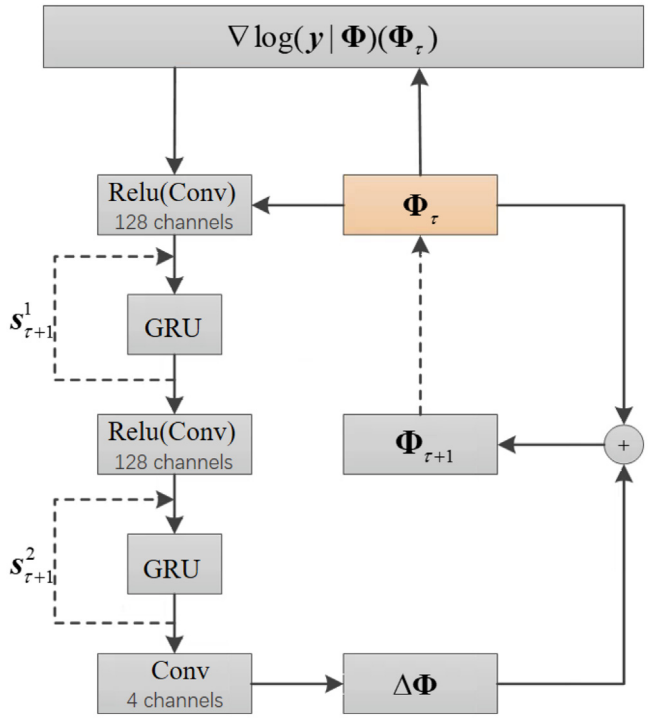

Fig. 2. The network architecture of the quantitative Recurrent Inference Machine.

then be obtained by taking the real and imaginary components of the estimated $\boldsymbol{R}$, respectively. The gradient of the log-likelihood $\log p(\boldsymbol{y}|\boldsymbol{\Phi})$ is now given as follows:

$$\begin{cases} \frac{\partial L}{\partial M} := \frac{1}{\sigma^2} \sum_{t=1}^{T} \sum_{c=1}^{C} \overline{\boldsymbol{R}} \odot \mathrm{e}^{-\mathrm{TE}_t} \odot \boldsymbol{\Lambda}, \\ \frac{\partial L}{\partial R} := -\frac{1}{\sigma^2} \sum_{t=1}^{T} \sum_{c=1}^{C} \mathrm{TE}_t \overline{\boldsymbol{M}} \odot \mathrm{e}^{-\mathrm{TE}_t \overline{\boldsymbol{R}}} \odot \boldsymbol{\Lambda}, \end{cases} \tag{8}$$

where $L = \log p(\boldsymbol{y}|\boldsymbol{\Phi})$, and $\boldsymbol{\Lambda} = \boldsymbol{S}_c^H \mathcal{F}^{-1} G^T (G \mathcal{F} \boldsymbol{S}_c \boldsymbol{x}_t - \boldsymbol{y}_{t,c})$. The operation $\cdot^H$ denotes the Hermitian conjugate and $\bar{\cdot}$ denotes the complex conjugate. The RIM implicitly learns the log-prior $\log p(\boldsymbol{\Phi})$ with the training data. To distinguish the RIM for quantitative parameter mapping from the network for image reconstruction purposes, we designate it as the quantitative RIM (qRIM).

The architecture of the model, depicted in Fig. 2, is built as follows. Each of the first two convolutional layers (Conv) is followed by the Rectified Linear Unit (ReLU) activation function and interleaved with the gated recurrent units (GRU) (Cho et al., 2014) which are used to maintain the internal state. This results in two internal states $\boldsymbol{s} = \{\boldsymbol{s}^1, \boldsymbol{s}^2\}$ for $\boldsymbol{s}$ in Eq. (7). The first convolutional layer is with 8 input channels (4 for the estimate of parameter maps $\boldsymbol{\Phi}_\tau$, and another 4 for the gradients of the log-likelihood for the estimate), 128 output channels, and kernel size of 5×5, whereas the second convolutional layer is with 128 input channels, 128 output channels, and kernel size of 3×3. Each GRU is with $2 \times (128 \times 384 + 384)$ parameters. The second GRU is followed by a third convolutional layer with 128 input channels, 4 output channels, kernel size of 3×3, and without bias terms. In total the network is with 376,064 parameters.

We chose to initialize $\boldsymbol{\Phi}_0$, an input to the qRIM network, with the fitted parameter maps using the conventional sequential models of image reconstruction and relaxation, as described in Section 5.

4. Quantitative end-to-end variational network

The extension of the unified forward model may also be adopted in other physics-based deep learning MRI reconstruction frameworks with unrolled optimization. For the purpose of comparison to the qRIM, we implemented the quantitative End-to-End Variational Network (qE2EVN). The qE2EVN extends the state-of-the-art E2EVN (Sriram et al., 2020) which solves the inverse problem of accelerated MRI reconstruction through unrolled optimization by gradient descent.

By defining the regularizer as a UNet, the qE2EVN iteratively performs updates for the optimization of Eq. (4) through a number of cascades, given by

$$\boldsymbol{\Phi}_{k+1} = \boldsymbol{\Phi}_k + \lambda r\left(\boldsymbol{S}_c^H \mathcal{F}^{-1} G^T \left(\log p(\boldsymbol{y}|\boldsymbol{\Phi}_k)\right)\right), \tag{9}$$

where k is the current cascade, and r is a regularizer weighted by a factor λ. The architecture of the model is presented in Fig. 3.

For the qE2EVN we chose 8 cascades of UNets, consisting of 18 channels and 4 pooling layers, while the padding size was set to 11. The selected hyperparameters were taken from Karkalousos et al. (2022), where extensive hyperparameters search was performed. The resulting number of trainable parameters was 19.6×10^6. The source code of qE2EVN is made available online.[1]

5. Experiments

5.1. Dataset

Data were selected from the AHEAD brain database (Alkemade et al., 2020), covering the adult life span with a uniform age range distribution between 21 and 81 years of age. The Institutional Review Board approval and informed consent from the volunteers were obtained. The MP2RAGE-ME (Magnetization Prepared 2 Rapid Acquisition Gradient Echoes Multi Echo) sequence (Caan et al., 2019) with FatNav motion navigators (Bazin et al., 2020c) was used for 3D acquisitions on a Philips 7T scanner equipped with a 32-channel Nova Medical head coil (Wilmington MA, USA). The sequence parameters include bandwidth = 405 Hz, $\mathrm{TR}_{\mathrm{MP2RAGEME}} = 6.8$ s, inversion times $\mathrm{TI}_1 = 0.67$ s and $\mathrm{TI}_2 = 3.7$ s, repetition times $\mathrm{TR}_1 = 6.2$ ms and $\mathrm{TR}_2 = 31$ ms, flip angle $= 4°$ for both readouts. The echo time of the single readout at the first inversion time was $\mathrm{TE}_1 = 3.0$ ms, and echo times of the four readouts at the second inversion time were $\mathrm{TE}_2 = [3.0, 11.5, 20.0, 28.5]$ ms. The matrix size was $292 \times 290 \times 234$ with a resolution of 0.7 mm isotropic. The acquisition was two-fold accelerated along one phase-encoding dimension and had a turbo factor of 150.

Before motion correction, the k-space data were GRAPPA-interpolated (Griswold et al., 2002). To account for translations and rotations between shots, FatNavs were rigidly coregistered, and the corresponding k-space lines per turbo shot were corrected. To this end, the translation parameters were converted into a phase factor by which k-space data were multiplied. Data were then rotated according to the estimated rotation parameters and regridded using a non-uniform Fast Fourier Transform (for details, see Bazin et al., 2020c). This reconstruction is referred to as the reference data in the later training of the network and evaluations of the methods.

Sensitivity maps to be used in the forward model of Eqs. (2) and (3) were acquired with an additional coil sensitivity reference scan. From this reference scan, coil sensitivities were estimated using autocalibration (Lustig et al., 2007). This scan matched the field of view of the MP2RAGE-ME sequence, with a flip angle of 6° and a resolution of 2.0 mm isotropic.

A total of 71 subjects were included in this study. In training, validation, and testing of the qRIM, 18, 2, and 10 subjects were used, respectively. Of each subject, a stack of 50 slices in the mid-brain was selected. For 3-fold cross-validation, the test set was cycled in the three folds over all subjects, and the training and validation subjects were randomly selected out of the remaining batch. For testing generalizability, we used

[1] https://github.com/wdika/mridc.

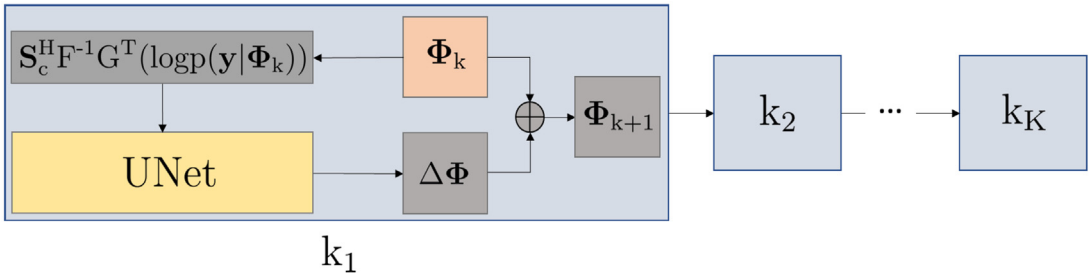

Fig. 3. The network architecture of the quantitative End-to-End Variational Network (qE2EVN). K is the total number of cascades.

a set of 42 subjects over a broad range from 19 to 80 years of age. Raw data of the AHEAD database is made available online.[2]

For R_2^* mapping, the four echoes of the second inversion data TE_2 were used. In this study, we focused on 2D R_2^* mapping, for which 2D k-space slices were extracted from the inverse Fourier-transformed reference 3D k-space of individual coil images in the readout direction.

The 2D k-space was retrospectively subsampled with variable density along both dimensions. The subsampling was with Gaussian pseudo-random patterns with a relative full width at half maximum of 0.7 times the acquisition matrix, and with a fraction of 0.02 fully sampled in the k-space center. Subsampling patterns varied per echo time and were generated with different random seeds (see Fig. 1).

5.2. Training

The reference maps acting as the ground-truth were obtained by least squares fitting (LSQ) on reference images of four echo times to Eq. (1). The phase of every echo time was unwrapped for fitting $\boldsymbol{B}_0$ (Abdul-Rahman et al., 2005).

The source code of the qRIM is made available online.[3] For training of the qRIM, structural similarity index measure (SSIM) (Wang et al., 2004) was computed as a loss metric of each time step. SSIM was computed over all estimated parameters $\boldsymbol{\Phi} = \{\boldsymbol{R}_2^*, \boldsymbol{M}, \boldsymbol{B}_0\}$. The final loss $l(\boldsymbol{\Phi}_T)$ is the average over all time steps as

$$l(\boldsymbol{\Phi}_T) = \frac{1}{T}\sum_{\tau=1}^{T}\sum_{\boldsymbol{\phi}\in\boldsymbol{\Phi}} \boldsymbol{\omega}_{\boldsymbol{\phi}}\mathrm{SSIM}(\boldsymbol{\Phi}_{\tau,\phi}\odot\boldsymbol{D}, \boldsymbol{\Phi}_{\phi}\odot\boldsymbol{D}), \tag{10}$$

where SSIM() computes the summation of SSIMs between the two inputs. $D \in \{0,1\}^P$ is a binary brain mask computed using SPM12 (Ashburner and Friston, 2005) in MATLAB (MathWorks, Natick, Massachusetts) on the magnitude image of the second echo time. Therefore, the loss $l(\boldsymbol{\Phi}_T)$ was effectively computed in the brain region only. For $\boldsymbol{M} \in \boldsymbol{\Phi}$ the SSIM was computed separately in real and imaginary channels. The SSIM of $\boldsymbol{R}_2^*$ was assigned with a higher weight with $\boldsymbol{\omega}_{\boldsymbol{R}_2^*} = 3$ than other parameters which are with $\boldsymbol{\omega}_{\{\Re e(\boldsymbol{M}),\Im m(\boldsymbol{M}),\boldsymbol{B}_0\}} = 1$.

Although parameter maps created with zero-filled reconstruction and subsequent LSQ can act as the initialized input for qRIM, a better initialization is usually preferred to ease the learning and improve the network output. Therefore, a single RIM for image reconstruction (Lønning et al., 2019) was trained on data of individual echoes from the training data specified above. The model specifications were the same as in Lønning et al. (2019) with the SSIM as loss metric. This trained RIM was used to independently reconstruct all echo time images from the subsampled data. The initialized parameter maps for the qRIM were computed with LSQ of these reconstructions to Eq. (1). We refer to this initialization method as RIM + LSQ in the rest of the paper. For all networks that are used in this work, the training lasted until their training loss was stabilized.

[2] https://doi.org/10.34894/IHZGQM.

[3] https://github.com/chaopingzhang/qRIM.

5.3. Comparison methods

Four methods were selected for comparison. First, a conventional non-deep learning approach was adopted, being the widely used Compressed Sensing image reconstruction with LSQ (CS + LSQ). The CS reconstruction was performed using the BART toolbox (Lustig et al., 2007) with regularization on the $l1$-norm of the wavelet coefficients with the regularization factor 0.01. The regularization factor was selected for an optimal root mean squared error (RMSE) with the reference $\boldsymbol{R}_2^*$ map while avoiding excessive noise.

Second, a different network architecture, being the U-Net was included for evaluation. The U-Net model was adapted for parameter mapping, with the same architecture as described in Ronneberger et al. (2015) except that we used four input channels and four output channels to fit our application. This network was initialized in the same way as qRIM and was also trained with the same SSIM as the loss metric.

Third, the RIM + LSQ was used. As introduced above for initialization of the qRIM, this method has separate image reconstruction and parameter estimation. Fourth, the qE2EVN described in Section 4 as another physics-based deep learning method that unrolls an optimization was included in comparison to the qRIM. The qE2EVN used the same initialization as qRIM.

5.4. Evaluations

Besides the visual comparison of the $\boldsymbol{R}_2^*$ maps among all methods, the RMSE was computed on $\boldsymbol{R}_2^*$ maps for all testing subjects. Because the Structural Similarity Index (SSIM) and peak signal-to-noise ratio (PSNR) are widely adopted in the image reconstruction field, they were computed alongside the RMSE.

To test for an effect of reconstruction model on $\boldsymbol{R}_2^*$ and $\boldsymbol{B}_0$, two-way analysis of variance (ANOVA) was performed for the RMSE per acceleration factor. Post-hoc tests were conducted to test for differences between pairs of models. To test for an increasing improvement in performance with acceleration factor, the RMSE difference between RIM + LSQ and qRIM, i.e. $\triangle$RMSE, was computed for different acceleration factors. Subsequently, the linear trend of $\triangle$RMSE as a function of acceleration factor was computed for all subjects and statistically tested using a one-sample signed t-test.

To assess the variability of RMSE over subjects, we conducted a 3-fold cross-validation (see Section 5.1). To constrain the training time, this cross-validation was conducted for 12-times accelerated data only. Mean and standard deviation of $\triangle$RMSE were computed and tested using a one-sample signed t-test.

We conducted an ablation study to evaluate the effect of k-space sampling over different echo times (TEs). In addition to variable sampling over TEs, we performed the qRIM prediction with identical k-space patterns. We quantified a possibly reduced reconstruction performance using the same testing subjects, and computed the RMSE of the predicted $\boldsymbol{R}_2^*$ maps with regards to the reference maps.

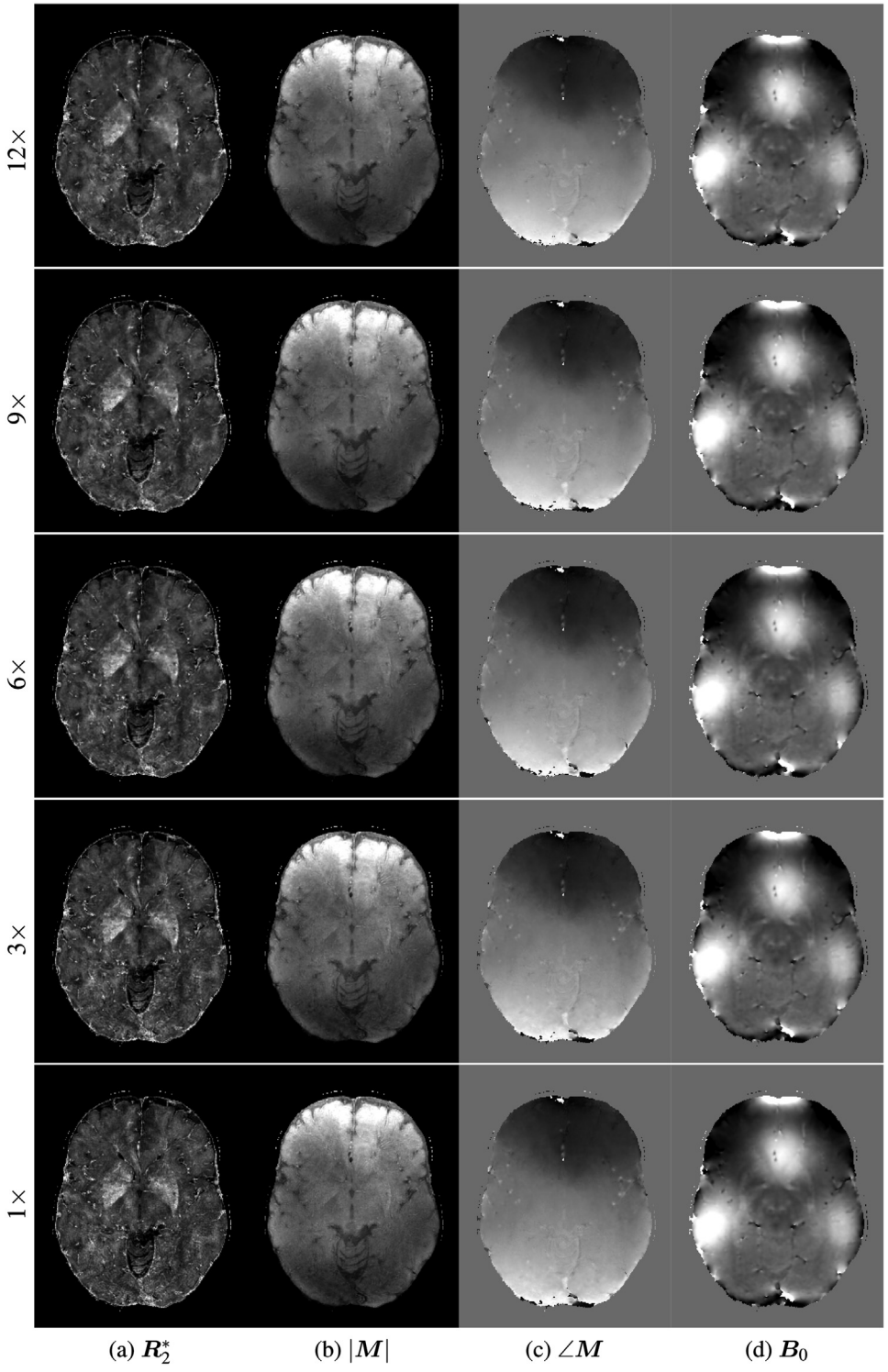

Fig. 4. The maps of Φ_T: R_2^*, $|M|$, $\angle M$, and B_0 of the qRIM with acceleration factors of 3, 6, 9, and 12, and the corresponding reference maps from fully sampled data.

While the qRIM model was trained and validated with pseudo-random subsampling k-space patterns, we did extra predictions on data with the commonly used equidistance subsampling patterns to test the generalization ability of qRIM.

To evaluate accuracy and precision of the methods in selected regions of interest (ROIs) in the subcortex, the mean and standard deviation (std) of the reconstruction errors, i.e., the difference with regard to the reference, were computed within the thalamus (Tha), the red nucleus (RN), the substantia nigra (SN), the subthalamic nucleus (STN), and the striatum (Str) for all methods. These sub-cortical brain regions are most relevant in the clinical context of e.g. deep brain stimulation (Isaacs et al., 2020). The segmentations of Tha, RN, SN, STN, and Str were computed using the MASSP algorithm (Bazin et al., 2020b) of the NighRes toolbox (Huntenburg et al., 2018) on reference reconstructions of the same subjects from the AHEAD database (Alkemade et al., 2020).

Finally, we studied the extent to which subcortical maturation effects are preserved by the qRIM for increasing acceleration factors. The striatum is known to show a strong linear correlation between the in-

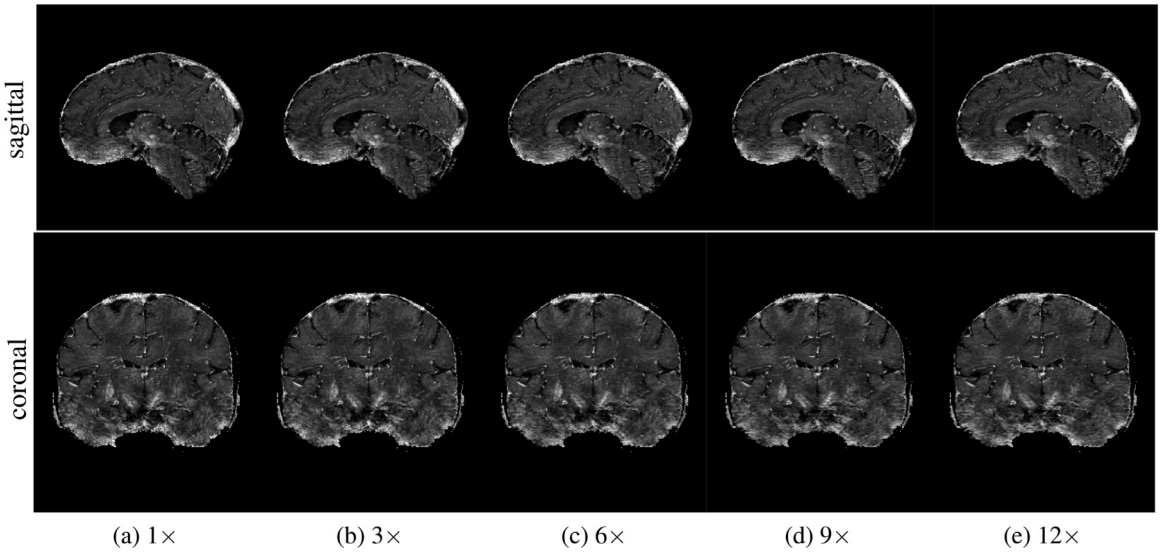

Fig. 5. The sagittal and coronal planes of R_2^* of the qRIM with acceleration factors of 3, 6, 9, and 12, and the corresponding reference R_2^* (1×) from fully sampled data.

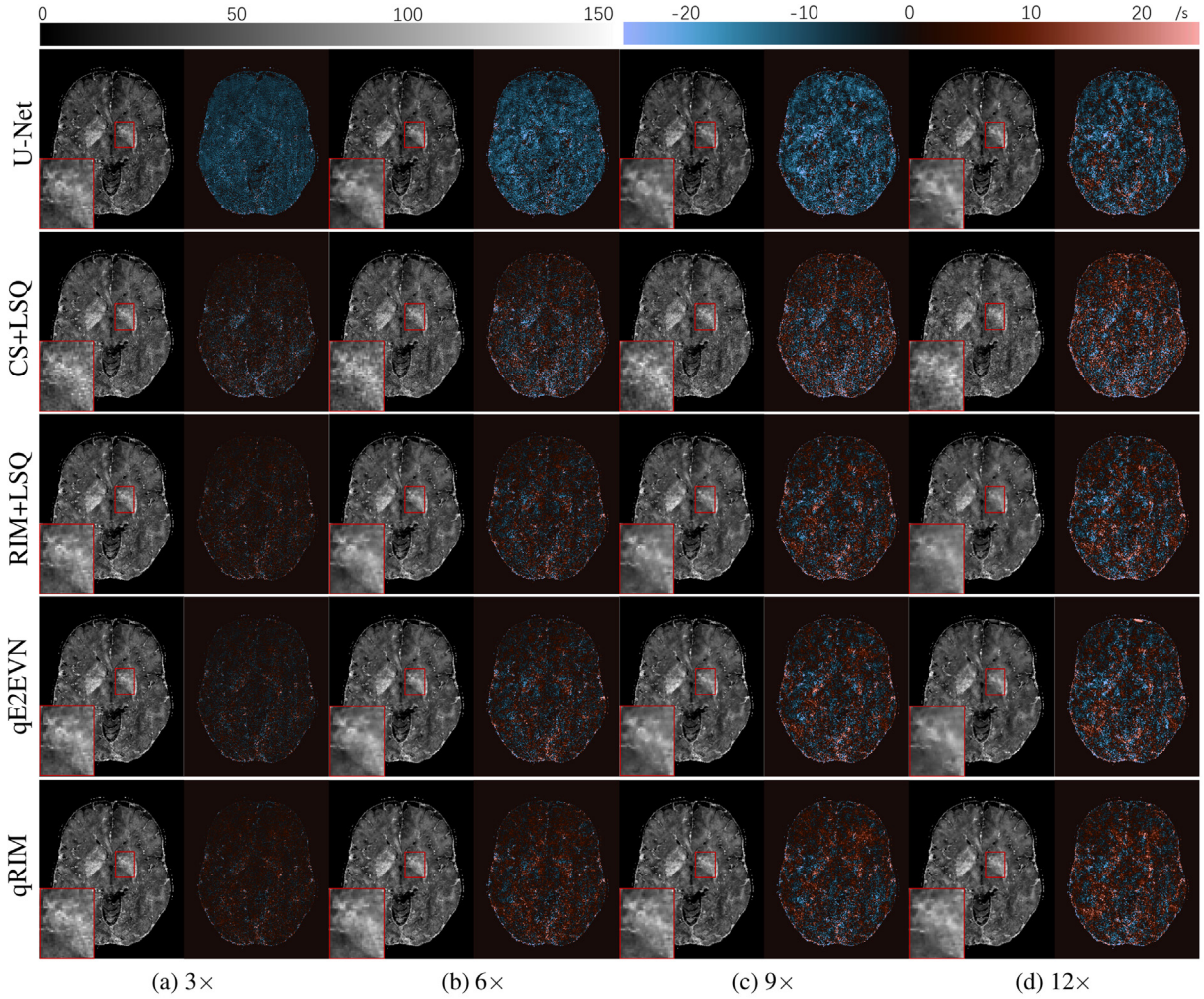

Fig. 6. Example R_2^* maps of the U-Net, CS + LSQ, RIM + LSQ, qE2EVN, and qRIM, with acceleration factors of (a) 3, (b) 6, (c) 9, (d) 12, and the difference images with regard to the reference next to each R_2^* map. The R_2^* map (1×) in Fig. 4 shows the reference map.

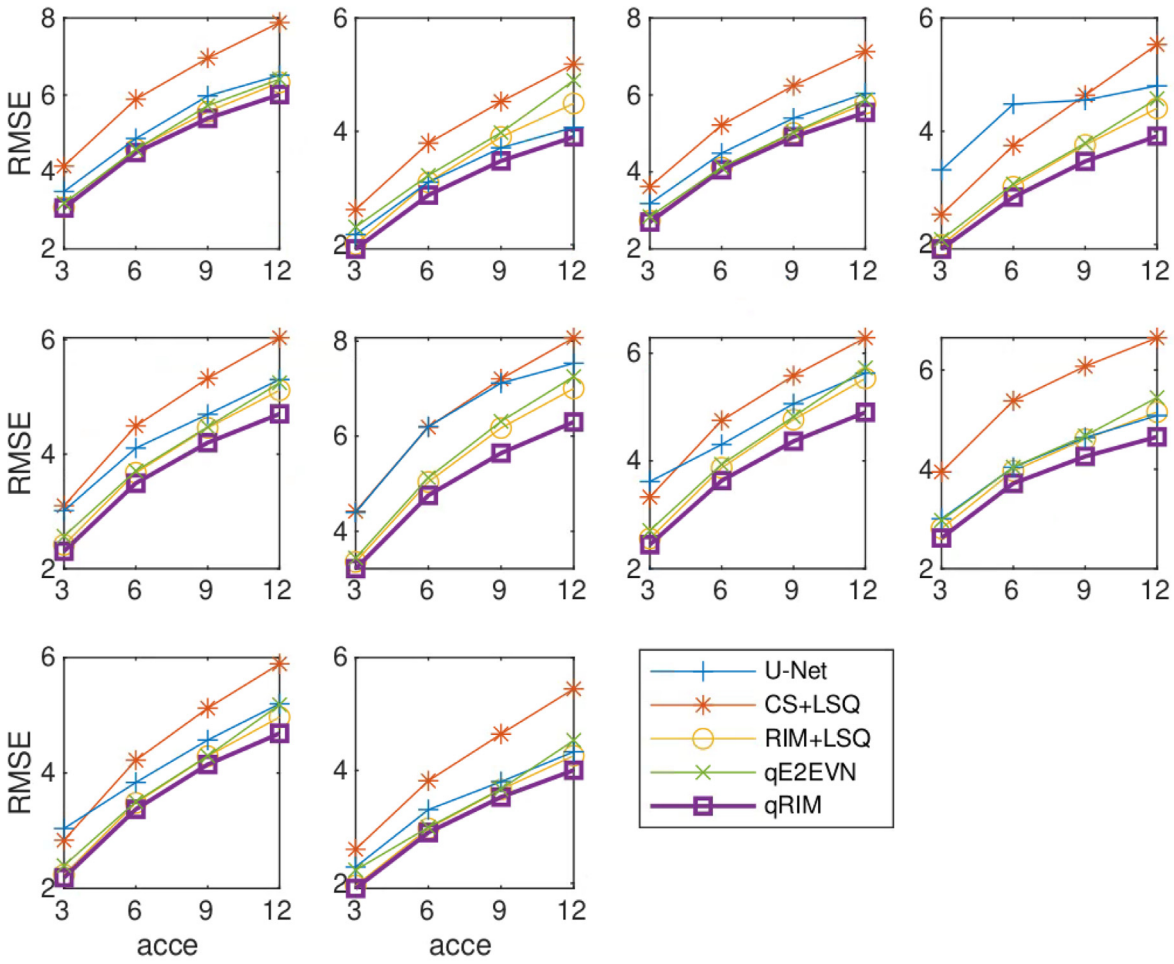

Fig. 7. RMSE of $\boldsymbol{R}_2^*$ as a function of acceleration factor (acce) for CS + LSQ, U-Net, RIM + LSQ, qE2EVN, and qRIM. Each plot refers to data of a single test subject.

terquartile range (IQR) of $\boldsymbol{R}_2^*$ and age (Miletić et al., 2022), related to local iron deposition. A linear fit of the IQR of $\boldsymbol{R}_2^*$ as a function of age was computed for the mapping from qRIM, RIM + LSQ, and the reference data. In this experiment, the $\boldsymbol{R}_2^*$ maps of 42 subjects were computed. This independent test dataset had no intersection with neither the training nor the validation set. The distribution of the age of these subjects covers a wide range from 19 to 80 years of age.

6. Results

The maps of $\boldsymbol{\Phi}_T$, i.e. $\boldsymbol{R}_2^*$, $|\boldsymbol{M}|$, $\angle\boldsymbol{M}$, and $\boldsymbol{B}_0$ of the proposed qRIM are shown in Fig. 4, with multiple acceleration factors for one axial slice of one selected subject, as well as the reference maps (with 1× acceleration). The $\boldsymbol{R}_2^*$ map shows expected contrasts and the $\boldsymbol{M}$ map shows expected magnitude and phase. The $\boldsymbol{B}_0$ map also shows the expected off-resonance pattern in the frontal and temporal regions of the brain. A stable parameter fit has been observed for all acceleration factors. Fig. 5 shows the sagittal and coronal planes of the qRIM predicted $\boldsymbol{R}_2^*$ maps.

Fig. 6 shows the same axial slice of the $\boldsymbol{R}_2^*$ maps for all methods with all acceleration factors and the error images with regard to the reference map next to each reconstruction. Visually, with a higher acceleration factor, the image appears as more blurred. The U-Net results show the most biased $\boldsymbol{R}_2^*$, and the RIM + LSQ and the qRIM achieved better $\boldsymbol{R}_2^*$ maps with less error than the CS + LSQ. The qEVEVN results show similar quality to the RIM + LSQ results but are with sharper details for 12-fold acceleration. Compared to the RIM + LSQ, the $\boldsymbol{R}_2^*$ map of the qRIM shows less blurred image content, revealing the heterogeneous tissue properties. The images of more subjects are provided in supplementary material, and lead to the same observations as in Fig. 6.

Fig. 7 shows the RMSE of the $\boldsymbol{R}_2^*$ maps per subject as a function of acceleration factor for the comparison methods and the proposed qRIM model. Two-way analysis of variance (ANOVA) of the RMSE of $\boldsymbol{R}_2^*$ showed a significant effect of reconstruction methods ($p < 1 \times 10^{-4}$). Post-hoc analyses showed that the qRIM had a lower RMSE than RIM + LSQ for 9 and 12-fold acceleration ($p = 0.04$ and $p < 1 \times 10^{-4}$), but not for 3 and 6-fold acceleration ($p = 0.8$ and $p = 0.5$). The qRIM had lower RMSE than CS + LSQ and the U-Net for all acceleration factors. Comparing RIM + LSQ to U-Net, the U-Net was inferior up to 9-fold acceleration ($p < 1 \times 10^{-4}$, $p = 3 \times 10^{-4}$, $p = 0.02$ for 3, 6 and 9-fold acceleration), but not for 12-fold acceleration ($p = 0.44$). A two-way ANOVA of the RMSE of $\boldsymbol{B}_0$ also showed an effect of reconstruction methods ($p < 1 \times 10^{-8}$). The RMSE of $\boldsymbol{B}_0$ of the qRIM did not differ from CS + LSQ and RIM + LSQ, but was lower than the RMSE of the U-Net reconstruction ($p < 1 \times 10^{-4}$). The CS + LSQ and the U-Net show the largest RMSE, which agrees to the visual observation in Fig. 6. The RIM + LSQ has a lower RMSE than the U-Net for most subjects but consistently higher RMSE than the qRIM. The qEVEVN shows slightly higher RMSE than the RIM + LSQ. The SSIM is shown in Fig. S4 and the PSNR is shown in Fig. S5 in supplementary material. Both of them agree well to the RMSE results. In the ablation study into k-space sampling over TEs, the qRIM showed an increase in RMSE of $\boldsymbol{R}_2^*$ of 0.5% when using fixed instead of variable sampling patterns.

To assess the effect of acceleration in the two best performing methods, the $\triangle$RMSE between the RIM + LSQ and the qRIM as a function

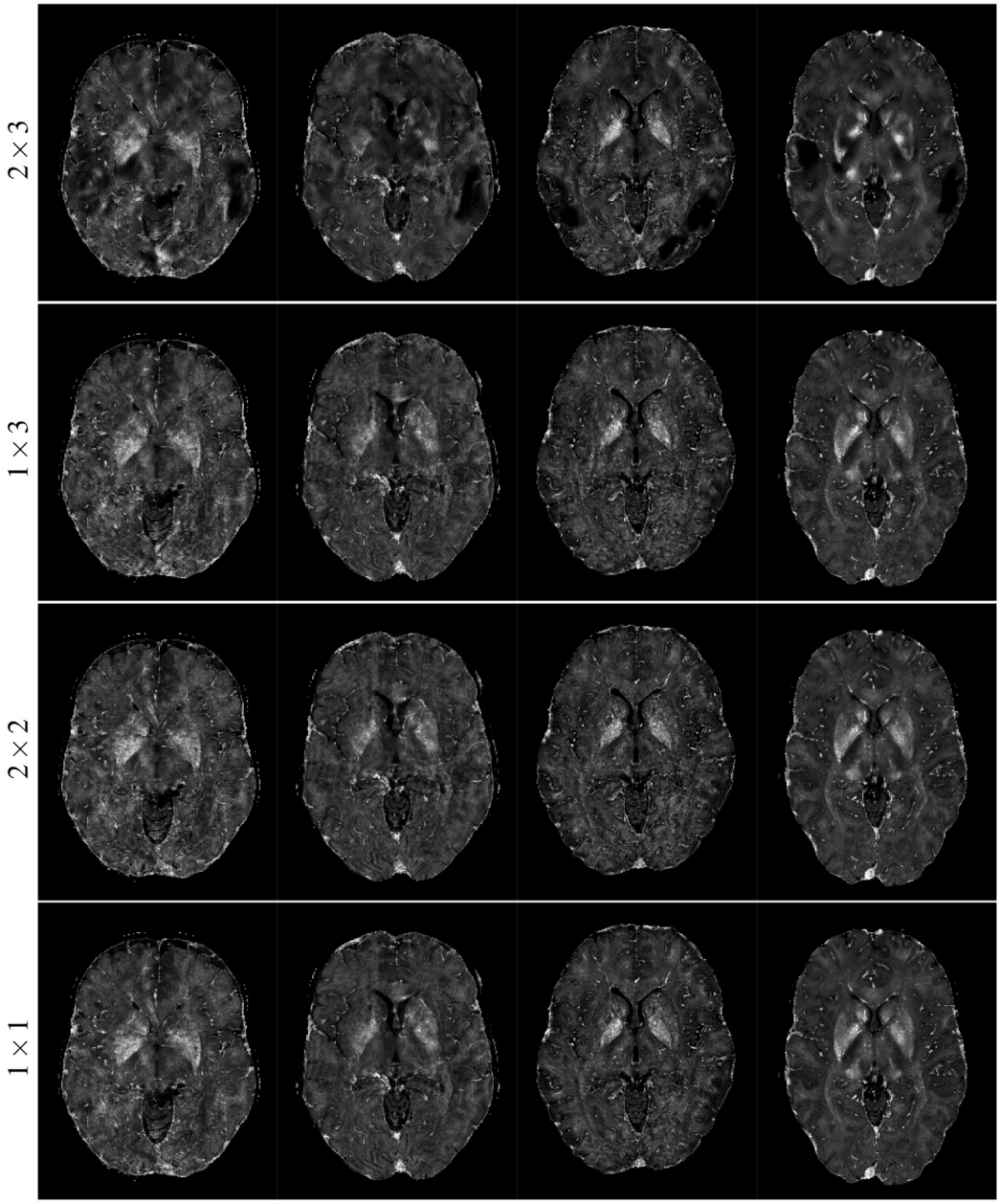

Fig. 8. The R_2^* maps predicted from data with equidistance subsampling patterns using the qRIM model trained with pseudo-randomly subsampled data. The R_2^* maps with acceleration factors of 2×2, 1×3, 2×3 and the reference maps (1×1) are shown for four testing subjects.

of acceleration factor is shown in Fig. 9 with error bars denoting the standard error of the mean. This shows that the RMSE reduction by qRIM over all subjects increases with the acceleration factor. The slope of the curve, depicting the improvement with acceleration factor, was found to be significantly larger than zero in a one-sample signed *t*-test ($p = 2 \times 10^{-4}$).

A 3-fold cross-validation experiment was then conducted on 12-fold accelerated data. Visual inspection showed ghosting artifacts due to motion in one subject and incorrect masking in an other, these two subjects were henceforth excluded from analysis. The mean and standard deviation for $\triangle$RMSE were 0.47 ± 0.28, 0.20 ± 0.26, and 0.45 ± 0.39. These differences were all statistically significant ($p < 1 \times 10^{-3}$, $p = 0.03$ and $p = 0.004$).

Fig. 8 shows the R_2^* maps predicted from data with equidistance subsampling patterns using the qRIM model trained with pseudo-randomly subsampled data. The results show good quality R_2^* maps with no visible aliasing artifacts for subsampling factors 2×2 and 1×3, and strong artifacts for 2×3.

Fig. 10 shows statistics on accuracy and precision in selected ROIs, for 12-fold acceleration. Fig. 10(a) shows that the qRIM is least biased among all the R_2^* reconstructions. The U-Net, the RIM + LSQ, and the qE2EVN underestimated R_2^* in all ROIs, while CS + LSQ has varying performance of the reconstruction accuracy over different ROIs. Fig. 10(b) indicates that among all methods, the reconstruction errors of CS + LSQ were with the lowest precision in all ROIs, which coincides with the error maps shown in Fig. 6.

Fig. 11 shows the linear fitting of IQR of R_2^* in the striatum as a function of age for the mapping from qRIM, RIM + LSQ, and the reference data. The qRIM experiences no bias in the offset and a negligible increase in slope of the curve until an acceleration factor of 9. The slope is slightly overestimated for 12-fold acceleration. For RIM + LSQ, the IQR fitting shows a negatively biased offset compared to the fitting to

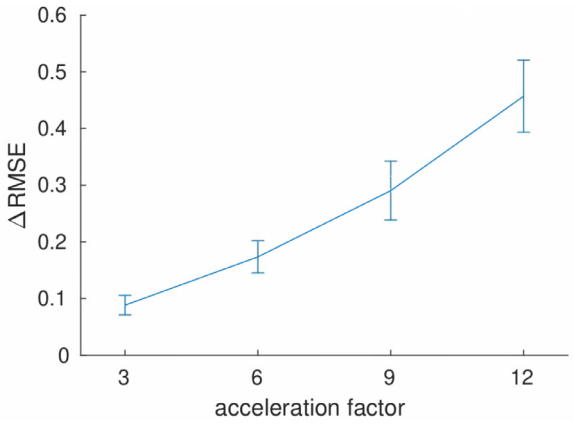

Fig. 9. The RMSE difference between RIM + LSQ and qRIM (i.e. ΔRMSE = RMSE(RIM + LSQ) - RMSE(qRIM)) as a function of acceleration factor with error bars denoting the standard error of the mean. Positive values yield an improvement of the proposed method.

the reference data. The magnitude of the bias increases with the acceleration factor.

7. Discussion

This paper presents the Recurrent Inference Machine for accelerated quantitative MRI (qRIM) in application to R_2^* mapping at 7T. A unified forward model of image reconstruction and signal relaxation is formulated and employed, allowing for jointly optimizing image reconstruction and parameter mapping. The proposed qRIM benefits from the shared knowledge between these two tasks and integrates them into the forward model.

These advantages become apparent in comparison to conventional sequential image reconstruction and parameter fitting (RIM + LSQ). The proposed method shows a reduced error in R_2^*, with an increasing improvement for higher acceleration factors. Specifically, the accuracy of all ROIs is preserved, while RIM + LSQ experiences a negative bias. Also, the qRIM qualitatively presents reduced image blur compared to the RIM + LSQ.

For the subcortical maturation, accumulating iron deposition leads to an increasingly heterogeneous appearance of the striatum and thereby an increase in the IQR of R_2^* with age (Miletić et al., 2022). With an increasing acceleration factor, it is increasingly more difficult to adequately reconstruct this heterogeneous texture. The smoothing as introduced by RIM + LSQ mapping led to an underestimated IQR of R_2^*, manifested as a negative bias in the fitting. This bias increased with the acceleration factor. In contrast, with preserved sharpness in the qRIM reconstruction of R_2^*, the fitting is unbiased up to an acceleration factor of 9. At a 12-fold acceleration, the SNR becomes low even for qRIM in older subjects due to increasing iron accumulation, leading to a noisier prediction and hence a marginal overestimation of the IQR of R_2^*.

The better performance of the qRIM could be explained by the R_2^*-relaxometry model included in the qRIM, which provides additional prior information. With this model, information across echo times can be shared during the reconstruction process. Hence, the proposed qRIM has additional spatial information compared to the RIM model which reconstructs each echo time image independently. Additionally, the convolutional nature of the RIM network allows learning spatial correlations within the receptive field which may stabilize the fitting compared to the independent voxel-wise estimation of LSQ. Another contributing factor to the increased performance could be that by initializing through the RIM + LSQ, the qRIM effectively has more iterations and capacity to learn.

The ablation study showed improved R_2^* mapping with variable k-space patterns over TEs compared to fixed patterns. Complementary phase encoding over TEs might attribute to the ability of the qRIM to reconstruct highly accelerated data.

In this study, pseudo-random subsampling k-space patterns were used and validated, because of the improved suppression of aliasing noise compared to equidistant subsampling (Lustig et al., 2008). While pseudo-random patterns have now been implemented for most vendors, equidistance subsampling patterns are still broadly used in the clinic. Our experiments with such patterns illustrate that the qRIM model trained with data using pseudo-random subsampling k-space patterns were able to reconstruct equidistance subsampled data with good quality images and R_2^* maps with no visible artifacts with acceleration factors of 2×2 and 1×3. For six-fold acceleration (2×3), the image quality was unacceptable with strong aliasing artifacts. The qRIM model thus generalizes to a certain extent to subsampling patterns unseen dur-

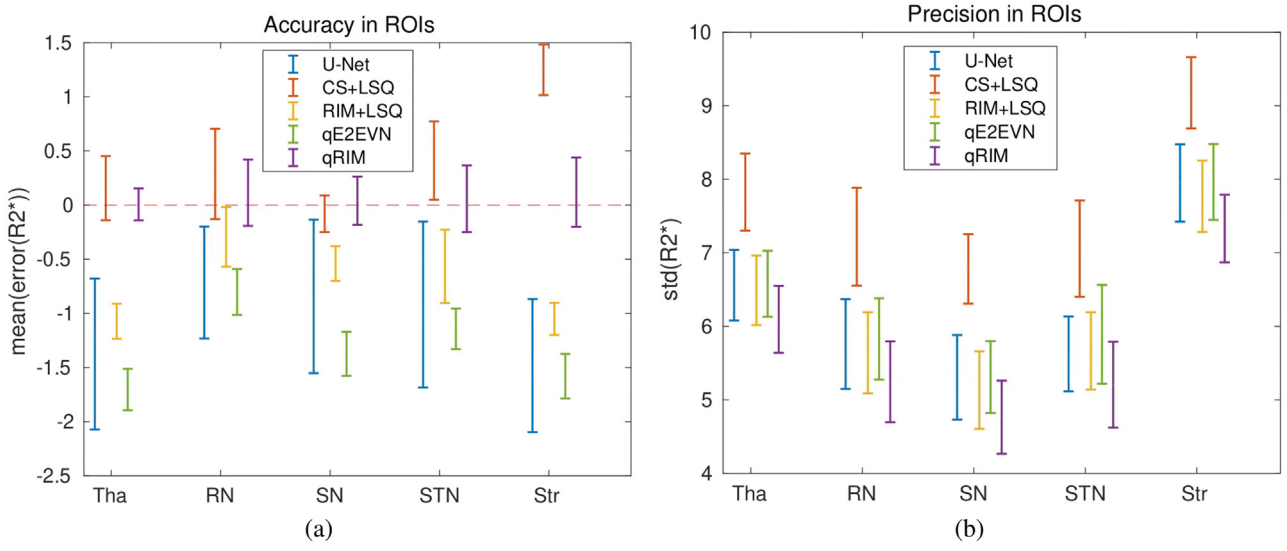

Fig. 10. The distribution over subjects of the mean (a) and the std (b) of reconstruction errors of the R_2^* in the ROIs: Thalamus (Tha), Red Nucleus (RN), Substantia Nigra (SN), Subthalamic Nucleus (STN), and Striatum (Str) with the acceleration factor of 12. Each bar is centered on the mean over subjects and extends from −1 to +1 times the std over subjects. The dashed red line in (a) indicates where the mean of the error is zero. (For interpretation of the references to color in this figure legend, the reader is referred to the web version of this article.)

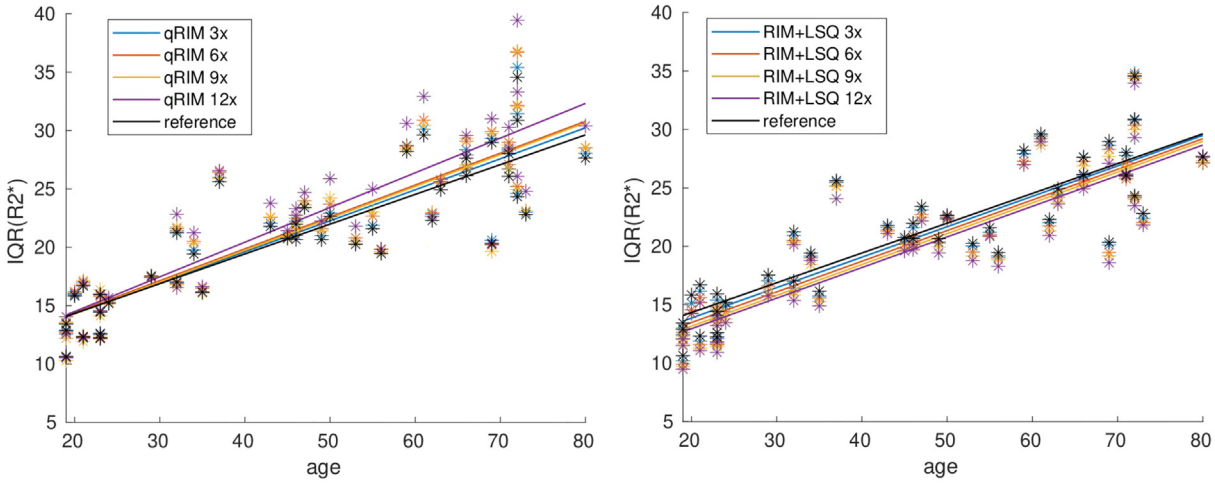

(a) IQR of R_2^* from qRIM vs age (b) IQR of R_2^* from RIM+LSQ vs age

Fig. 11. Linear fitting of the interquartile range (IQR) of R_2^* in the striatum as a function of age for the mapping from qRIM, RIM + LSQ, and the reference data.

ing training. Nevertheless, careful validation is still needed. We expect that models trained with equidistance subsampling patterns yield an improved outcome (Muckley et al., 2021).

When evaluating and comparing to another network structure, the U-Net performs worse than both qRIM and RIM + LSQ with an overall more biased estimation of R_2^*. The RMSE increase of the U-Net along the acceleration factors is inconsistent over different subjects, which suggests possible overfitting. Contrary to the U-Net, the RIM model has an iterative learning process through its recurrent network. The forward model of the inverse problem is used to compute the gradient of the log-likelihood in each iteration. This provides an assessment of how well the current step estimate fits the reconstruction process with the given measurements, and the RIM model learns to make use of this information in the iterative process. As has been validated in Lønning et al. (2019), with the benefits of robustness against overfitting, RIM requires relatively little data to train a good model. The provided training data seemed sufficient for the current qRIM and RIM + LSQ where no signs of overfitting emerged.

We also show that the proposed extension of the unified forward model is not limited to the RIM framework. With qE2EVN good quality R_2^* maps were reconstructed, although slightly inferior to the qRIM reconstruction. An advantage of the qRIM is that the gradient of log-likelihood is explicitly computed for the unrolled optimization and the data consistency is implicitly embedded in the network infrastructure, while in the qE2EVN the data consistency is performed explicitly. We expect the integration of the extended unified forward model to also work in other model-based deep networks that unroll an optimization, e.g., cascades of independently RIMs (Karkalousos et al., 2022).

The CS + LSQ, which is a non-deep learning method, shows overall the highest RMSE among all comparison methods (see Fig. 7), mainly caused by a significantly higher standard deviation of R_2^* in multiple ROIs (see Fig. 10). This makes the CS + LSQ inferior to the qRIM and the RIM + LSQ, and demonstrates the added value of learning from data for this application.

A practical limitation of the qRIM method for the specific R_2^* mapping problem is that the training of the qRIM needs to be constrained to the brain region, thus requiring a segmentation as a preprocessing step. This step is required because of otherwise observed phase wrapping in the skull region over successive TEs, such that the reference B_0 is ill-defined in this region. In the test stage, such a step is not needed, thereby minimizing the impact of the required segmentation.

Since all supervised methods are to some extent dependent on the training dataset and experience a domain shift problem, some fine tuning will be needed if the SNR changes due to resolution, field strength, or parameter shifts. That said, recent work demonstrated high robustness of the RIM to noise (Sabidussi et al., 2021).

Clinical populations (e.g., Parkinson's disease) might experience an increase in R2*, and thus even lower signal at high TE (Jorge et al., 2020). Therefore, sufficient SNR is crucial. We expect the trained model to be robust to reduced SNR (Sabidussi et al., 2021). A validation study will be needed to assess whether this observed robustness generalizes to simultaneous reconstruction and parameter estimation.

With the validated R_2^* mapping using the ME-GRE sequences, we expect to generalize this work to the mapping of other relaxometry parameter in future work that may serve various clinical applications. For this purpose, the forward models need to be customized, and the networks need to be retrained with different datasets. As an example, recent work showed that R1-mapping using deep learning is feasible (Jun et al., 2021).

Future work could investigate the applicability of R_2^* mapping in presurgical planning of Deep Brain Stimulation in Parkinson's patients. Another potential extension includes motion compensation. Motion is an important source of artifacts in qMRI (Zaitsev et al., 2015). Hence a potential extension to this work is to integrate a motion model in the forward model to reduce motion-induced artifacts.

8. Conclusions

The proposed qRIM using a unified forward model for reconstruction and parameter estimation can exploit the redundancy among TEs and shared knowledge between the two tasks thanks to the forward model. A stable reconstruction of R_2^* of the human subcortex up to 9-fold acceleration is achieved. Subcortical maturation can be reliably quantified over the life span. The qRIM thus allows for the reconstruction of more accurate parameters, with improved image sharpness compared to the conventional pathway.

Declaration of Competing Interest

M.W.A. Caan is shareholder of Nico-lab International Ltd.

Credit authorship contribution statement

Chaoping Zhang: Methodology, Software, Formal analysis, Writing – original draft, Visualization. **Dimitrios Karkalousos:** Methodology, Software, Formal analysis, Writing – original draft, Visualization.

Pierre-Louis Bazin: Methodology, Software, Formal analysis, Writing – review & editing, Visualization. **Bram F. Coolen:** Methodology, Writing – review & editing. **Hugo Vrenken:** Methodology, Writing – review & editing. **Jan-Jakob Sonke:** Methodology, Writing – review & editing. **Birte U. Forstmann:** Methodology, Writing – review & editing. **Dirk H.J. Poot:** Methodology, Conceptualization, Writing – review & editing. **Matthan W.A. Caan:** Conceptualization, Methodology, Funding acquisition, Software, Validation, Formal analysis, Supervision, Writing – original draft.

Data Availability

Quantitative motion-corrected 7T sub-millimeter raw MRI database of the adult lifespan https://doi.org/10.34894/IHZGQM

Acknowledgments

This work was partly supported by a NWO Vici (BUF), a ERC-CoG (BUF), and a NWO STW (BUF) grant. This publication is partly based on the STAIRS project under the TKI-PPP program. The collaboration project is co-funded by the PPP Allowance made available by Health Holland, Top Sector Life Sciences & Health, to stimulate public-private partnerships.

Supplementary material

Supplementary material associated with this article can be found, in the online version, at doi:10.1016/j.neuroimage.2022.119680

References

Abdul-Rahman, H., Gdeisat, M., Burton, D., Lalor, M., 2005. Fast three-dimensional phase-unwrapping algorithm based on sorting by reliability following a non-continuous path. In: Osten, W., Gorecki, C., Novak, E.L. (Eds.), Optical Measurement Systems for Industrial Inspection IV, International Society for Optics and Photonics. SPIE, pp. 32–40.

Aggarwal, H.K., Mani, M.P., Jacob, M., 2018. Modl: model-based deep learning architecture for inverse problems. IEEE Trans. Med. Imaging 38 (2), 394–405.

Alkemade, A., Mulder, M.J., Groot, J.M., Isaacs, B.R., van Berendonk, N., Lute, N., Isherwood, S.J., Bazin, P.L., Forstmann, B.U., 2020. The Amsterdam ultra-high field adult lifespan database (AHEAD): a freely available multimodal 7 Tesla submillimeter magnetic resonance imaging database. NeuroImage 221, 117200.

Andre, J.B., Bresnahan, B.W., Mossa-Basha, M., Hoff, M.N., Patrick Smith, C., Anzai, Y., Cohen, W.A., 2015. Toward quantifying the prevalence, severity, and cost associated with patient motion during clinical MR examinations. J. Am. Coll. Radiol. 12 (7), 689–695.

Ashburner, J., Friston, K.J., 2005. Unified segmentation. NeuroImage 26 (3), 839–851.

Bazin, P.-L., Alkemade, A., Mulder, M.J., Henry, A.G., Forstmann, B.U., 2020. Multi-contrast anatomical subcortical structures parcellation. elife 9, e59430.

Bazin, P.-L., Alkemade, A., Mulder, M.J., Henry, A.G., Forstmann, B.U., 2020. Multi-contrast anatomical subcortical structures parcellation. eLife 9, e59430.

Bazin, P.L., Nijsse, H.E., van der Zwaag, W., Gallichan, D., Alkemade, A., Vos, F.M., Forstmann, B.U., Caan, M.W., 2020. Sharpness in motion corrected quantitative imaging at 7T. NeuroImage 222, 117227.

Bilgic, B., Goyal, V.K., Adalsteinsson, E., 2011. Multi-contrast reconstruction with Bayesian compressed sensing. Magn. Reson. Med. 66 (6), 1601–1615.

Bilgic, B., Kim, T.H., Liao, C., Manhard, M.K., Wald, L.L., Haldar, J.P., Setsompop, K., 2018. Improving parallel imaging by jointly reconstructing multi-contrast data. Magn. Reson. Med. 80 (2), 619–632.

Caan, M.W., Bazin, P.L., Marques, J.P., de Hollander, G., Dumoulin, S.O., van der Zwaag, W., 2019. MP2RAGEME: T1, T2*, and QSM mapping in one sequence at 7 Tesla. Hum. Brain Mapp. 40 (6), 1786–1798.

Caballero, J., Price, A.N., Rueckert, D., Hajnal, J.V., 2014. Dictionary learning and time sparsity for dynamic MR data reconstruction. IEEE Trans. Med. Imaging 33 (4), 979–994.

Chatnuntawech, I., Martin, A., Bilgic, B., Setsompop, K., Adalsteinsson, E., Schiavi, E., 2016. Vectorial total generalized variation for accelerated multi-channel multi-contrast MRI. Magn. Reson. Imaging 34 (8), 1161–1170.

Cho, K., Van Merriënboer, B., Gulcehre, C., Bahdanau, D., Bougares, F., Schwenk, H., Bengio, Y., 2014. Learning phrase representations using RNN encoder-decoder for statistical machine translation. arXiv preprint arXiv:1406.1078

Ding, L., Gold, J.I., 2013. The basal Ganglia's contributions to perceptual decision making. Neuron 79 (4), 640–649.

Doneva, M., Börnert, P., Eggers, H., Stehning, C., Sénégas, J., Mertins, A., 2010. Compressed sensing reconstruction for magnetic resonance parameter mapping. Magn. Reson. Med. 64 (4), 1114–1120.

Ehrhardt, M.J., Betcke, M.M., 2016. Multicontrast MRI reconstruction with structure-guided total variation. SIAM J. Imaging Sci. 9 (3), 1084–1106.

Gregor, K., LeCun, Y., 2010. Learning fast approximations of sparse coding. In: Proceedings of the 27th International Conference on International Conference on Machine Learning, pp. 399–406.

Griswold, M.A., Jakob, P.M., Heidemann, R.M., Nittka, M., Jellus, V., Wang, J., Kiefer, B., Haase, A., 2002. Generalized autocalibrating partially parallel acquisitions (GRAPPA). Magn. Reson. Med. 47 (6), 1202–1210.

Haldar, J.P., 2013. Low-rank modeling of local k-space neighborhoods (LORAKS) for constrained MRI. IEEE Trans. Med. Imaging 33 (3), 668–681.

Haldar, J.P., Hernando, D., Liang, Z.-P., 2011. Compressed-Sensing MRI with random encoding. IEEE Trans. Med. Imaging 30 (4), 893–903.

Hammernik, K., Klatzer, T., Kobler, E., Recht, M.P., Sodickson, D.K., Pock, T., Knoll, F., 2018. Learning a variational network for reconstruction of accelerated MRI data. Magn. Reson. Med. 79 (6), 3055–3071.

Huang, Y., Paisley, J., Lin, Q., Ding, X., Fu, X., Zhang, X.-P., 2014. Bayesian nonparametric dictionary learning for compressed sensing MRI. IEEE Trans. Image Process. 23 (12), 5007–5019.

Huntenburg, J.M., Steele, C.J., Bazin, P.L., 2018. Nighres: processing tools for high-resolution neuroimaging. GigaScience 7 (7), 1–9.

Isaacs, B.R., Keuken, M.C., Alkemade, A., Temel, Y., Bazin, P.-L., Forstmann, B.U., 2020. Methodological considerations for neuroimaging in deep brain stimulation of the subthalamic nucleus in parkinson's disease patients. J. Clin. Med. 9 (10), 3124.

Jorge, J., Gretsch, F., Najdenovska, E., Tuleasca, C., Levivier, M., Maeder, P., Gallichan, D., Marques, J.P., Bach Cuadra, M., 2020. Improved susceptibility-weighted imaging for high contrast and resolution thalamic nuclei mapping at 7T. Magn. Reson. Med. 84 (3), 1218–1234.

Jun, Y., Shin, H., Eo, T., Kim, T., Hwang, D., 2021. Deep model-based magnetic resonance parameter mapping network (DOPAMINE) for fast T1 mapping using variable flip angle method. Med. Image Anal. 102017.

Karkalousos, D., Noteboom, S., Hulst, H.E., Vos, F.M., Caan, M.W., 2022. Assessment of data consistency through cascades of independently recurrent inference machines for fast and robust accelerated MRI reconstruction. Phys. Med. Biol. 67 (12), 124001.

Keuken, M.C., Isaacs, B.R., Trampel, R., Van Der Zwaag, W., Forstmann, B., 2018. Visualizing the human subcortex using ultra-high field magnetic resonance imaging. Brain Topogr. 31 (4), 513–545.

Knoll, F., Murrell, T., Sriram, A., Yakubova, N., Zbontar, J., Rabbat, M., Defazio, A., Muckley, M.J., Sodickson, D.K., Zitnick, C.L., Recht, M.P., 2020. Advancing machine learning for MR image reconstruction with an open competition: overview of the 2019 fastMRI challenge. Magn. Reson. Med. 84 (6), 3054–3070.

Kopanoglu, E., Güngör, A., Kilic, T., Saritas, E.U., Oguz, K.K., Çukur, T., Güven, H.E., 2020. Simultaneous use of individual and joint regularization terms in compressive sensing: joint reconstruction of multi-channel multi-contrast MRI acquisitions. NMR Biomed. 33 (4), e4247.

Kreutz-Delgado, K., 2009. The complex gradient operator and the CR-calculus. arXiv preprint arXiv:0906.4835

Küstner, T., Würslin, C., Gatidis, S., Martirosian, P., Nikolaou, K., Schwenzer, N., Schick, F., Yang, B., Schmidt, H., 2016. MR image reconstruction using a combination of compressed sensing and partial Fourier acquisition: ESPReSSo. IEEE Trans. Med. Imaging 35 (11), 2447–2458.

Lee, D., Jin, K.H., Kim, E.Y., Park, S.-H., Ye, J.C., 2016. Acceleration of MR parameter mapping using annihilating filter-based low rank Hankel matrix (ALOHA). Magn. Reson. Med. 76 (6), 1848–1864.

Liang, D., Cheng, J., Ke, Z., Ying, L., 2020. Deep magnetic resonance image reconstruction: inverse problems meet neural networks. IEEE Signal Process. Mag. 37 (1), 141–151.

Liu, F., Feng, L., Kijowski, R., 2019. MANTIS: model-augmented neural neTwork with incoherent k-space sampling for efficient MR parameter mapping. Magn. Reson. Med. 82 (1), 174–188.

Lønning, K., Putzky, P., Sonke, J.-J., Reneman, L., Caan, M.W., Welling, M., 2019. Recurrent inference machines for reconstructing heterogeneous MRI data. Med. Image Anal. 53, 64–78.

Lustig, M., Donoho, D., Pauly, J.M., 2007. Sparse MRI: the application of compressed sensing for rapid MR imaging. Magn. Reson. Med. 58 (6), 1182–1195.

Lustig, M., Donoho, D.L., Santos, J.M., Pauly, J.M., 2008. Compressed sensing MRI. IEEE Signal Process. Mag. 25 (2), 72–82.

Lustig, M., Pauly, J.M., 2010. SPIRiT: iterative self-consistent parallel imaging reconstruction from arbitrary k-space. Magn. Reson. Med. 64 (2), 457–471.

Maier, O., Schoormans, J., Schloegl, M., Strijkers, G.J., Lesch, A., Benkert, T., Block, T., Coolen, B.F., Bredies, K., Stollberger, R., 2019. Rapid T1 quantification from high resolution 3D data with model-based reconstruction. Magn. Reson. Med. 81 (3), 2072–2089.

Miletić, S., Bazin, P.-L., Isherwood, S.J., Keuken, M.C., Alkemade, A., Forstmann, B.U., 2022. Charting human subcortical maturation across the adult lifespan with in vivo 7 T MRI. NeuroImage 249, 118872.

Mink, J.W., 1996. The basal ganglia: focused selection and inhibition of competing motor programs. Prog. Neurobiol. 50 (4), 381–425.

Muckley, M.J., Riemenschneider, B., Radmanesh, A., Kim, S., Jeong, G., Ko, J., Jun, Y., Shin, H., Hwang, D., Mostapha, M., Arberet, S., Nickel, D., Ramzi, Z., Member, S., Ciuciu, P., Member, S., Starck, J.-l., Teuwen, J., Karkalousos, D., Zhang, C., Sriram, A., Huang, Z., Yakubova, N., Lui, Y.W., Florian, K., 2021. Results of the 2020 fastMRI challenge for machine learning MR image reconstruction. IEEE Trans. Med. Imaging 40 (9), 2306–2317.

O'Doherty, J., Dayan, P., Schultz, J., Deichmann, R., Friston, K., Dolan, R.J., 2004. Dissociable roles of ventral and dorsal striatum in instrumental conditioning. Science 304 (5669), 452–454.

Pruessmann, K.P., Weiger, M., Scheidegger, M.B., Boesiger, P., 1999. SENSE: sensitivity encoding for fast MRI. Magn. Reson. Med. 42 (5), 952–962.

Putzky, P., Welling, M., 2017. Recurrent inference machines for solving inverse problems. arXiv preprint arXiv:1706.04008

Ravishankar, S., Bresler, Y., 2010. MR image reconstruction from highly undersampled k-space data by dictionary learning. IEEE Trans. Med. Imaging 30 (5), 1028–1041.

Ronneberger, O., Fischer, P., Brox, T., 2015. U-net: convolutional networks for biomedical image segmentation. In: International Conference on Medical Image Computing and Computer-Assisted Intervention. Springer, pp. 234–241.

Rueda, A., Malpica, N., Romero, E., 2013. Single-image super-resolution of brain MR images using overcomplete dictionaries. Med. Image Anal. 17 (1), 113–132.

Sabidussi, E.R., Klein, S., Caan, M.W., Bazrafkan, S., den Dekker, A.J., Sijbers, J., Niessen, W.J., Poot, D.H., 2021. Recurrent inference machines as inverse problem solvers for MR relaxometry. Med. Image Anal. 74, 102220.

Schlemper, J., Caballero, J., Hajnal, J.V., Price, A.N., Rueckert, D., 2017. A deep cascade of convolutional neural networks for dynamic MR image reconstruction. IEEE Trans. Med. Imaging 37 (2), 491–503.

Schultz, W., Dayan, P., Montague, P.R., 1997. A neural substrate of prediction and reward. Science 275 (5306), 1593–1599.

Sriram, A., Zbontar, J., Murrell, T., Defazio, A., Zitnick, C.L., Yakubova, N., Knoll, F., Johnson, P., 2020. End-to-end variational networks for accelerated MRI reconstruction. In: Lecture Notes in Computer Science (including subseries Lecture Notes in Artificial Intelligence and Lecture Notes in Bioinformatics), vol. 12262. LNCS, pp. 64–73.

Stüber, C., Morawski, M., Schäfer, A., Labadie, C., Wähnert, M., Leuze, C., Streicher, M., Barapatre, N., Reimann, K., Geyer, S., Spemann, D., Turner, R., 2014. Myelin and iron concentration in the human brain: aquantitative study of MRI contrast. NeuroImage 93 (P1), 95–106.

Tezcan, K.C., Baumgartner, C.F., Luechinger, R., Pruessmann, K.P., Konukoglu, E., 2019. MR image reconstruction using deep density priors. IEEE Trans. Med. Imaging 38 (7), 1633–1642.

Tofts, P., 2005. Quantitative MRI of the Brain: Measuring Changes Caused by Disease.

Uecker, M., Lai, P., Murphy, M.J., Virtue, P., Elad, M., Pauly, J.M., Vasanawala, S.S., Lustig, M., 2014. ESPIRiT–an eigenvalue approach to autocalibrating parallel MRI: where SENSE meets GRAPPA. Magn. Reson. Med. 71 (3), 990–1001.

Wang, S., Cheng, H., Ying, L., Xiao, T., Ke, Z., Zheng, H., Liang, D., 2020. DeepcomplexMRI: exploiting deep residual network for fast parallel MR imaging with complex convolution. Magn. Reson. Imaging 68, 136–147.

Wang, Y., Ying, L., 2014. Compressed sensing dynamic cardiac cine MRI using learned spatiotemporal dictionary. IEEE Trans. Biomed. Eng. 61 (4), 1109–1120.

Wang, Z., Bovik, A.C., Sheikh, H.R., Simoncelli, E.P., 2004. Image quality assessment: from error visibility to structural similarity. IEEE Trans. Image Process. 13 (4), 600–612.

Zaitsev, M., Maclaren, J., Herbst, M., 2015. Motion artifacts in MRI: a complex problem with many partial solutions. J. Magn. Reson. Imaging 42 (4), 887–901.

Zhan, Z., Cai, J.-F., Guo, D., Liu, Y., Chen, Z., Qu, X., 2015. Fast multiclass dictionaries learning with geometrical directions in MRI reconstruction. IEEE Trans. Biomed. Eng. 63 (9), 1850–1861.

Zhang, C., Klein, S., Cristobal-Huerta, A., Hernandez-Tamames, J.A., Poot, D.H., 2021. APIR4EMC: autocalibrated parallel imaging reconstruction for extended multi-contrast imaging. Magn. Reson. Imaging 78 (February), 80–89.

Zhang, X., Guo, D., Huang, Y., Chen, Y., Wang, L., Huang, F., Xu, Q., Qu, X., 2020. Image reconstruction with low-rankness and self-consistency of k-space data in parallel MRI. Med. Image Anal. 63, 101687.